Mg-Exchanged Gismondine for Superior CO2/N2 and CO2/CH4 Separations

Jaouad Al Atrach, Igor Golub, Edwin Clatworthy, Jérôme Rey, Ying Xiong, Ayoub Daouli, Marie Desmurs, Michael Badawi, Rémy Guillet-Nicolas, Valentin Valtchev

Mg-exchanged Gismondine for superior CO_2/N_2 and CO_2/CH_4 separations

Jaouad al Atrach,[a] Igor E. Golub,[a] Edwin B. Clatworthy,[a] Jérôme Rey,[a] Ying Xiong,[a] Ayoub Daouli,[b] Marie Desmurs,[a] Michael Badawi,[b] Rémy Guillet-Nicolas,[a] Valentin Valtchev[a*]*

[a]Université de Normandie, ENSICAEN, UNICAEN, CNRS, Laboratoire Catalyse et Spectrochimie (LCS), Caen, 14050, France

[b]Université de Lorraine, CNRS, Laboratoire de Physique et Chimie Théoriques (LPCT), Nancy, F-54000, France

ABSTRACT

The CO_2 adsorption performance of a zeolite is related to the framework structure and extra-framework composition. In this work, parent Na-GIS and partially-exchanged NaMg1-GIS and NaMg3-GIS, with 30% and 50% degree of Mg^{2+} exchange, respectively, were prepared. Further, the series of zeolites were thoroughly characterized and studied for their applicability for CO_2 adsorption and CO_2/N_2 and CO_2/CH_4 separation by single component adsorption and dynamic breakthrough curve analysis methods. The lower concentration of Mg^{2+} cations in NaMg1-GIS resulted in enhanced CO_2 adsorption due to a beneficial distortion of the framework pore structure, making the adsorption of N_2 and CH_4 more challenging. However, this benefit was lost for higher Mg^{2+} concentration (NaMg3-GIS) due to a more pronounced framework distortion, impairing not only the adsorption of N_2 and CH_4 but also the CO_2 one, ultimately leading to a loss of selectivity. The molecular dynamics simulations and DFT calculations, aligning with

experimental data, reveal an elevated heat of adsorption for CO_2 in NaMg3-GIS due to framework deformation caused by Mg^{2+} cations. Consistent with the adsorption equilibrium experiments, the ternary dynamnic experiments of CO_2/N_2/He evaluated by breakthrough curve analysis show a higher CO_2/N_2 selectivity of 1673 and 1248 at 25 and 50 °C, respectively, for the NaMg1-GIS sample. For the CO_2/CH_4/He experiments, the CO_2/CH_4 selectivity tended towards extremely high values, due to negligible CH_4 uptake on NaMg1-GIS. In addition, the better dynamic adsorption/separation of CO_2 on NaMg1-GIS is ascribed to the greater distortion of the pore aperture due to the presence of Mg^{2+} cations, affecting the diffusion of small molecules. Overall, our results demonstrate the high potential of NaMg-GIS materials for critically important energy separation processes involving CO_2, N_2, and CH_4.

1. Introduction

Increasing global temperatures due to rising levels of atmospheric CO_2 from human activity is a major concern.[1] Post-combustion and direct air capture of CO_2 are examples of strategies to help mitigate the effects of rising CO_2 levels.[2] However, the presence of other gases such as N_2, O_2, H_2S and H_2O vapour in flue gas and air mixtures makes efficient CO_2 separation quite challenging.[3] Chemical absorption is the standard practice for CO_2 separation in industrial processes involving aqueous solutions of amines.[4] However, pollution, high cost, equipment corrosion, and difficulty of recycling these solvents pose significant problems.[5] Therefore, CO_2 separation based on microporous physical adsorbents has been considered a promising alternative technology.[6] Among such physical adsorbents, aluminosilicate zeolites exhibit several positive features, such as high thermal and chemical stability, high storage capacity, and selectivity with low synthesis cost.[7] However, the formation of chemisorbed species and a strong affinity for water require energy-intensive regeneration. Out of more than 250 known zeolites, small-pore

zeolites possessing pore windows of eight-membered rings (8MR, constructed from 8 T-atoms, T = Si, Al) have been found to yield the highest CO_2/N_2 and CO_2/CH_4 selectivities calculated from single component adsorption isotherms.[8] Since the window diameter of small-pore zeolites is comparable to the kinetic diameter of the targeted small gas molecules, an adjustment to the size of the 8MRs can allow the selective separation of CO_2 over larger molecules (N_2 and CH_4), being described as molecular sieving. Such separation capability is also influenced by the change of the electrostatic field within the zeolite through the control of the Si/Al ratio and the charge-compensating cations.[9–13] Furthermore, small pore zeolites were generally reported to exhibit a higher heat of adsorption due to the stronger CO_2-framework interactions, based on the modeling of pure-silica zeolites.[14]

The presence and type of extra-framework cations in aluminosilicate small-pore zeolites strongly influence the local environment of adsorption sites and the subsequent heat of adsorption strength, ultimately conditioning the overall adsorption behavior. Indeed, the size and the charge of cations influence the electric field, the acid-base properties, the size of the 8MR pore aperture, and the micropore volume of zeolites.[15–18] Several studies have investigated the effect of alkali-metal and alkaline-earth metal cations. It was reported that increasing the cation size results in higher Lewis basicity of the zeolite tailoring the CO_2 adsorption behavior.[19] Larger cations like Cs^+ and K^+ were found to afford the best CO_2 selectivity over N_2 and CH_4 in high aluminum chabazite (Si/Al < 3) due to the molecular trapdoor effect.[20 21] In comparison, smaller cations (*e.g.*, Li^+ and Na^+) may permit a higher CO_2 capacity due to their higher charge density and stronger interaction with CO_2.[18] For KFI zeolite with a Si/Al = 4.7 exchanged with different cations (H^+, Li^+, Na^+, K^+, Mg^{2+}, and Ca^{2+}), Li-KFI was found to provide the highest CO_2 uptake.[22] However, under industrially relevant conditions, CO_2 separation using physical

adsorbents such as zeolites is performed in a fixed bed configuration under dynamic conditions where the separation performance of adsorbents is dictated by the capacity, selectivity, and cyclability. Hence, despite being scarcely reported for novel laboratory-scale adsorbents,[23–26] breakthrough measurements are mandatory to properly understand and evaluate the practical application of zeolitic adsorbents.

In addition, among the variety of interesting zeolites, one less commonly studied for CO_2 separation is Gismondine (GIS). GIS is a natural zeolite with a Si/Al ratio of 1, also commonly known as maximal aluminum P (MAP) zeolite.[27] This zeolite is typically found in sodium,[28] sodium-potassium,[29] and calcium,[30] exchanged forms, and recently discovered in strontium form.[31] Zeolite P with a gismondine (GIS) framework type is among the zeolites with the highest structural flexibility.[32] It contains a three-dimensional pore system comprised of 8MR channels with a pore diameter of ca. 3.0 Å.[33] The framework distortion generates two isotypes, P1 and P2, resulting in different pore sizes and shapes. All double-crankshaft chains (dcc) in P1 crystals are aligned in the same direction, whereas P2 crystals exhibit alternating dcc chains that are misaligned by ± 15 ° of rotation. This slight change in the orientation of dcc chains leads to a narrower 8-MR pore aperture for P2 compared to P1, even if the pore networks remain similar.[34] Among 18 zeolites studied, force-field simulations have shown the all-silica GIS framework as the best topology for CO_2 adsorption.[14] Nevertheless, some physisorption measurements have claimed that both isotypes with a Si/Al ratio < 2 did not exceed a CO_2 uptake of 0.04 mmol/g at 25 °C and 1 bar,[34] which was later attributed to the strong "cation gating" effect resulting in the blocking of the 8MR apertures.[35] In the same study, a higher CO_2 uptake (3.7 mmol/g) was obtained for high silica GIS (Si/Al = 3.0), indicating that the aluminum content controls the CO_2 adsorption behavior in the framework. Herein, we investigate a new unexplored candidate for

separating CO_2/N_2 and CO_2/CH_4 gas mixtures, Mg-exchanged Gismondine. The synergistic effects arising from the combination of the structural flexibility of the GIS framework and the distinct properties of the Mg^{2+} cations found in different porous materials, such as exchanged magnesium ZK-5, CHA, and Mg-MOF, make Mg-exchanged Gismondine a very promising candidate for CO_2 adsorption applications.[22,36,37] This study examines in detail the impact of partial cation exchange within GIS zeolite on the equilibrium and dynamic CO_2 adsorption properties, and on the CO_2/N_2 and CO_2/CH_4 sorption and breakthrough curve analyses to evaluate the CO_2 adsorption capacity and CO_2/N_2 and CO_2/CH_4 selectivities, alongside competitive adsorption studies using DFT calculations at 0 K to discriminate the best cations and ab initio molecular dynamics simulations to compute adsorption enthalpies at finite temperature. Our results demonstrate the high potential of NaMg-GIS materials for critically important energy separation processes involving CO_2, N_2, and CH_4 and that a tailored modulation of the extra-framework cations type and content plays an essential role in CO_2 adsorption and separation.

2. Materials and Methods

2.1 Materials

Sodium hydroxide solution (NaOH, Thermo scientific, 50 wt% suspension, 99.5%), aluminium metal powder (Al, Alfa Aesar, 99.5%), colloidal silica Ludox HS-40 (SiO_2, Sigma-Aldrich, 40 wt% suspension, 99.9%) and Magnesium nitrate ($Mg(NO_3)_2$, Sigma-Aldrich, 99.0%) were used as received. Quartz fine granular (200–800 µm) was employed for blank breakthrough measurements. All water used was deionized using an Aquatron water still A4000D.

2.2 Synthesis

Zeolite Na-GIS was prepared with a gel composition of 0.5 Al_2O_3: 10 SiO_2: 3.0 Na_2O: 220 H_2O using the method described by Choi *et al.*[18] The typical procedure of the synthesis involves

starting with the mixing of sodium hydroxide with deionized water and stirring for 1 h at room temperature. Then, the aluminium powder was added, and the mixture was kept stirring for the following 2 h. Next, Ludox HS-40 was dissolved in water and added dropwise to the clear solution under agitation. During the whole process, the above mixture was kept in ice. The mixture was then aged overnight at room temperature, transferred to a Teflon-lined autoclave, and heated at 150 °C in a rotating oven for 1 day. Finally, the sample was recovered using centrifugation, washed with deionized water (4 times), and dried overnight at 60 °C.

2.3 Ion-exchange

Zeolite GIS, obtained in its sodium form (Na-GIS) as described above, was partially ion-exchanged with Mg^{2+}. A magnesium nitrate solution (1 M, 150 ml) was added to 3 g of zeolite sample, and the solution was heated to 80 °C and stirred at 500 rpm for 3 h. The initial pH of the solution was adjusted to a range of 5.3−5.5 prior to exchange with zeolite. The resulting product was collected, washed with deionized water (4 times), and dried at 60 °C overnight. The Mg-exchanged GIS zeolites are designated as NaMgx-GIS, where x indicates the number of times the cation exchange procedure is conducted.

2.4 General characterization

Phase identification and crystallinity were analysed using powder X-Ray diffraction (PXRD) on a PANalytical X'Pert Pro diffractometer with CuKα_1 radiation (λ = 1.5406 Å, 45 kV, 40 mA). The samples were scanned from 5 to 50 ° (2 theta) with a step size of 0.0167113 and a time per step of 2100 s. Using the same diffractometer in Bragg-Brentano geometry, variable-temperature (30, 150, 300 and 500 °C) PXRD experiments were carried out under air. The scan ranged from 5 to 40 ° with a step size of 0.0004363 and 475.32 as time per step.

Morphology analysis of the zeolite samples was performed using scanning electron microscopy (Tescan Mira I LMH) and was recorded using an acceleration voltage of 30 kV. Before measurement, samples were prepared by depositing < 1 mg of the powder on specimen holders using double-sided sticky tape and coating with Pt using the CRESSINGTON 108 auto sputter coater. Energy-dispersive X-ray spectroscopy (EDS) analysis of samples was performed using two Bruker XFLASH 6/30 detectors. The EDS analyses were conducted at a 15 kV accelerating voltage, 6−8 A probe current, and with an acquiring time of 5 minutes. The sample preparation method for EDS analysis was similar to SEM analysis, and no coating step was applied. Chemical analysis of samples was determined through inductively-coupled plasma mass spectrometry (ICP-MS) utilizing a 7900 ICP-MS from Agilent technologies. It is noteworthy that, in our study, ICP-MS served as the principal method for establishing elemental composition. EDS analysis was employed subsequently to validate and confirm the results obtained through ICP-MS. Thermal analysis (TG-DTG) was recorded on a Setsys Evolution (SETARAM). Analysis was carried out in flowing air from 30 to 1000 °C with a flow rate of 40 ml/min and a heating rate of 10 °C/min.

^{27}Al and ^{29}Si MAS NMR experiments were performed using a Bruker AVANCE 500 NB spectrometer with a rotational speed of 12 KHz. ^{27}Al MAS NMR was carried out at 130.30 MHz with a 4 mm probe head. $AlCl_3$ was used as a reference for the chemical shift. The experiment collected 2048 scans using a $\pi/6$ pulse with a radiofrequency field (rf) strength of 107 KHz, along with 1 s recycle delay. In the case of ^{29}Si MAS NMR, experiments were acquired at 99.35 MHz with the same 4 mm probe head. The total collected scans were 256 at $\pi/6$ pulse with a rf field strength of 38 KHz along with 20 s. TMS served as the reference for the chemical shift.

2.5 Equilibrium Adsorption Measurements

2.5.1 Single component gas adsorption measurements:

N_2 physisorption isotherms at −196 °C were performed using a Micromeritics 3Flex high resolution surface characterization analyzer unit. Prior to measurement, about 100 mg of sample was degassed at 300 °C under vacuum for 6 h. CO_2, N_2 and CH_4 physisorption isotherms at 0, 25 and 50 °C from 0–1.0 bar were measured with a Micromeritics ASAP2020 instrument. Degassing was performed on samples at 300 °C under high vacuum for 6 h before analysis. The isosteric enthalpy of adsorption (ΔH_{ads}) of CO_2 was calculated using Langmuir-Freundlich equation in OriginPro 8.5 software.

2.5.2 Dynamic Breakthrough Adsorption Measurements

Breakthrough measurements were performed using a 3P instrument SHP eco and a Cirrus-3 Quadrupole Mass Spectrometer, as described in earlier work.[38] The zeolite samples were prepared as pellets by loading powder between two core dice in a 20 mm die sleeve with a base plate and plunger and increasing the applied pressure to ~1.5 tonnes. The pellets were crushed and sieved into the desired fraction of 250–500 µm. Initially, a stainless-steel column with an inner diameter of 6 mm, containing the zeolite sample covered with glass wool, was subjected to a flow of He. Then, the zeolite samples were heated at 10 °C/min to 350 °C and held for 6 h under helium flow (20 mL min^{-1}). Prior to activation, TG analysis was conducted to measure the weight loss of water throughout the activation process. Once activated, the column contained 0.325 g of Na-GIS and 0.450 g of NaMg1-GIS. After activation, the zeolite samples were kept under He flow (20 mL.min^{-1}) at 25 °C before starting the breakthrough curve measurements.

Two ternary mixtures of $CO_2/N_2/He$ and $CO_2/CH_4/He$ (CO_2, N_2, and CH_4 as analytical components with He as carrier gas) at 1 bar were used. The flow rate of the individual

components for the simulated flue gas mixture of CO_2/N_2/He were 2, 10, and 28 mL.min^{-1}, respectively (total flow rate of 40 mL min^{-1}), representing 5, 25 and 70% of the feed composition for the adsorption step. The flow rate of the individual components for the simulated natural gas mixture of CO_2/CH_4/He were 4, 6, and 10 mL.min^{-1}, respectively (total flow rate of 20 mL.min^{-1}), representing 20, 30 and 50% of the feed composition for the adsorption step. Using a bypass line, the ternary mixtures were calibrated with a mass spectrometer. Once the temperature and spectrometer signals were stable, the gas stream flowing through the column was switched from pure He to the desired feed mixture. After a determined period of time whereby saturation of the adsorbent bed was reached, a desorption step was launched by switching the feed composition to 100% He with a flow rate of 40 mL.min^{-1} for the CO_2/N_2 and 20 mL.min^{-1} for CO_2/CH_4 separation experiments, respectively. The temperature remained constant for both the adsorption and desorption steps in each experiment; experiments were conducted at 25 and 50 °C by immersing the column in a water bath isothermally maintained by a chiller. The adsorption and desorption steps were conducted for 30 and 60 min, allowing sufficient time for the bed to reach equilibrium after the breakthrough. Fast cycling of breakthrough curve measurements consisting of five cycles with 100 s of adsorption and 300 s of desorption were performed. These measurements were carried out using the same experimental conditions that were used in the CO_2/N_2 and CO_2/CH_4 breakthrough experiments reaching saturation. Using a pressure sensor located immediately before the column and a pressure controller positioned immediately after the column, the pressure drop across the loaded column was determined. The pressure drops observed in all experiments were less than 0.07 bar or 6% of the column pressure.

The calculation of the adsorbed amounts of molecules was performed using the mixSorb Manager software. The adsorption capacity of adsorbates (CO_2, N_2, and CH_4) was determined based on the integrated areas illustrated in Figure S1 and S2.

$$n_{\text{adsorbed}} = \int V_{\text{in}}(t)c_{\text{in}}(t)dt - \int V_{\text{out}}(t)c_{\text{out}}(t)dt \quad \textbf{Eq. 1}$$

The advanced computed flow rate changes were employed to account for changes in the flow rate using the He carrier gas as an internal standard.

$$V_{\text{out}}(t) = \frac{V_{\text{He}}(t)}{1-\sum_{i=1}^{n} y_{\text{adsorptive},i}(t)} \quad \textbf{Eq. 2}$$

Blank breakthrough curves using identical conditions (gas mixture composition, temperature, flow rate) were measured on granular quartz to account for the adsorbed amounts in the free space between the adsorbent particles. The calculated loadings were subtracted from the values calculated for the zeolite samples while accounting for the mass of the adsorbent (Figure S3).

The calculated CO_2/N_2 (15:85, v/v) and CO_2/CH_4 (40:60, v/v) selectivities for both equilibrium and dynamic experiments were calculated using the following equation:

$$S_{ads} = (q_i/q_j)/(p_i/p_j) \quad \textbf{Eq. 3}$$

In this equation, q_i and q_j are the equilibrium molar uptakes of component i and j, while p_i and p_j are the partial pressure of the latter components.

2.6 Structural and computational details

2.6.1 Structural Model

To support our choice of the extra framework cations, we used Choi *et al.*'s model of the P2 polymorph of Gismondine,[18] because upon activation (in dehydrated conditions and at high temperatures), the P1 form is transformed into P2 polymorph (Figure S4). The P2 cell contains 48

222 atoms in its silicic form (16 T sites and 32 O). With a Si/Al ratio of 3 and extra-framework
223 sodium cations, the molecular formula is $Na_4Al_4Si_{12}O_{32}$. The cell parameters are the following: a
224 = 9.574 Å, b = 10.203 Å, c = 8.981 Å; $\alpha = 90.00°$, $\beta = 91.02°$, $\gamma = 90.00°$, following the $P2_1/n$
225 space group. The unit-cell volume is 877.153 $Å^3$.
226 The atomic positions were optimized, and the most stable configuration was identified after a
227 molecular dynamic run of 20 ps. The structure of the P2 polymorph of $Na_4Al_4Si_{12}O_{32}$ is shown in
228 Figure 1a and b.
229 The model for NaMg-P2 polymorph of GIS (50% of exchange) was built by the replacement of
230 two Na^+ cations (among the four Na^+ of the unit cell) with one Mg^{2+}. The twelve possible
231 structures were optimized, and the most stable one was reoptimized after a MD run of 20 ps. This
232 cell is shown in Figure 1c and d.

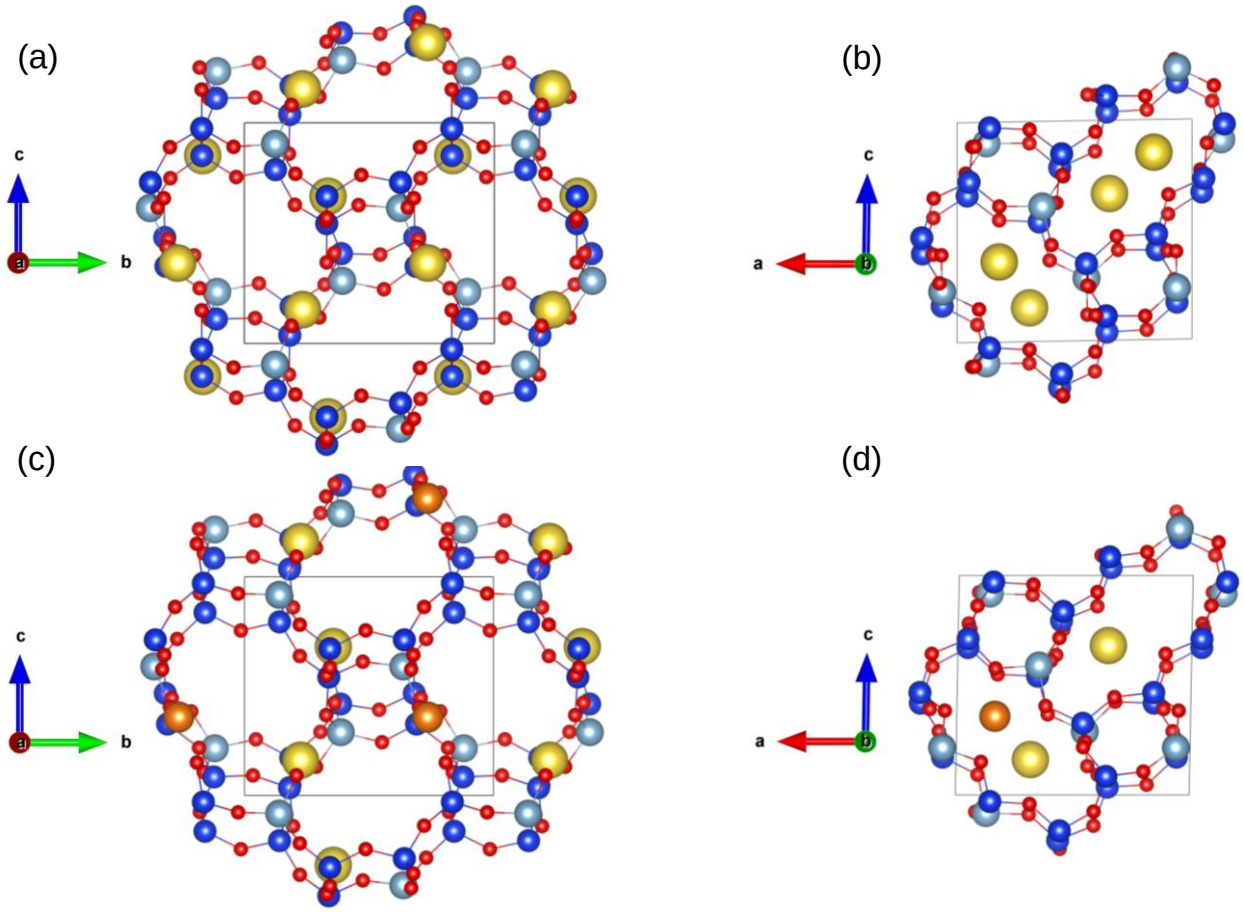

Figure 1. P2 polymorph of Na-GIS (a, b) and NaMg-GIS (c, d) is shown in two directions. Color code: Si in blue, O in red, Al in light blue, Na^{+} in yellow, and Mg^{2+} in orange.

2.6.2 Computational details

All periodic density functional theory (DFT) calculations were performed with the Vienna *Ab Initio* Simulation Package (VASP) code,[39–41] with the projector augmented plane wave (PAW) method developed by Blöchl[42] and adjusted by Kresse and Joubert.[43] The semilocal Perdew-Burk-Ernzehof (PBE) functional[44] was used. Due to the use of relatively large cells, we restricted the Brillouin zone sampling to the Γ-point as we are working with rather large cells. The convergence criterion for the electronic self-consistent cycle was set 10^{-7} eV, and the plane wave cutoff kinetic energy to 600 eV.

The long-range dispersion interactions were described with the D3 correction of Grimme[45] with Becke-Johnson damping.[46] This simple approach is known for its accuracy in modeling zeolite chemistry, and its low computational cost made it affordable for molecular dynamics simulations.[47,48]

Molecular dynamics simulations have been performed in the NVT ensemble with the same settings, except that the electronic convergence criterion was increased to 10^{-6} eV. The temperature of 300 K was maintained by the Andersen thermostat[49] with a collision frequency per atom of 0.01 per step. The integration step was 0.5 fs.

To compute adsorption enthalpies, the convergence of the potential energy of each system was carefully checked (with independence of the mean and variance over a long period), and the standard error on the mean was estimated after block averaging.[50] Equilibration periods were of at least 10 ps and production periods of at least 90 ps.

Molecular dynamics simulations with 0 to 4 CO_2 molecules per cell were performed to compute successive enthalpies of adsorption of CO_2, which can be considered as isosteric adsorption enthalpies at different coverages.[51] One molecule per cell corresponds to 0.94 mmol/g for Na-GIS and 0.96 mmol/g for NaMg-GIS.

The successive adsorption enthalpies, for the following reaction:

$$(CO_2)_{n-1}/GIS + 1\ CO_{2(g)} = (CO_2)_n/GIS,$$

with *n* varying from 1 to 4, were computed as follows:

$$\Delta H_{succ} = \langle E_{(CO_2)_n/GIS} \rangle - \langle E_{(CO_2)_{n-1}/GIS} \rangle - \langle E_{CO_2} \rangle - RT, \qquad \textbf{Eq. 4}$$

where $\langle E_{(CO_2)_n/GIS} \rangle$, $\langle E_{(CO_2)_{n-1}/GIS} \rangle$ and $\langle E_{CO_2} \rangle$ are, respectively, ensemble averages of the total energies of *n* and (*n* – 1) adsorbed CO_2 molecules in Na- or NaMg-GIS and the CO_2 molecule in gas phase.

3. Results and discussion

3.1 Adsorption energies on Na-GIS and NaMg-GIS

The choice to use Mg^{2+} cation to partially exchange the Na-GIS sample was directed by the results of static DFT calculations where the adsorption energies of CO_2, CH_4, and N_2 in Na-GIS and NaMg-GIS (50% exchanged), at T = 0 K, were computed using the following equation:

$$\Delta E_{ads} = E_{GIS+mol} - E_{GIS} - E_{mol}, \quad \textbf{Eq. 5}$$

where E_{GIS} is the energy of Na- or NaMg-GIS; E_{mol} the energy of the isolated molecule in the gas phase; and $E_{GIS+mol}$ the energy of the adsorbed molecule in Na- or NaMg-GIS.

Different initial positions of the adsorbed molecules were tried, and molecular dynamics runs of 30 ps were performed to identify the most stable configurations. The results are shown in Figure 2, and the corresponding values are reported in Table S1. The most stable adsorption configurations of CO_2 are represented in Figure S5.

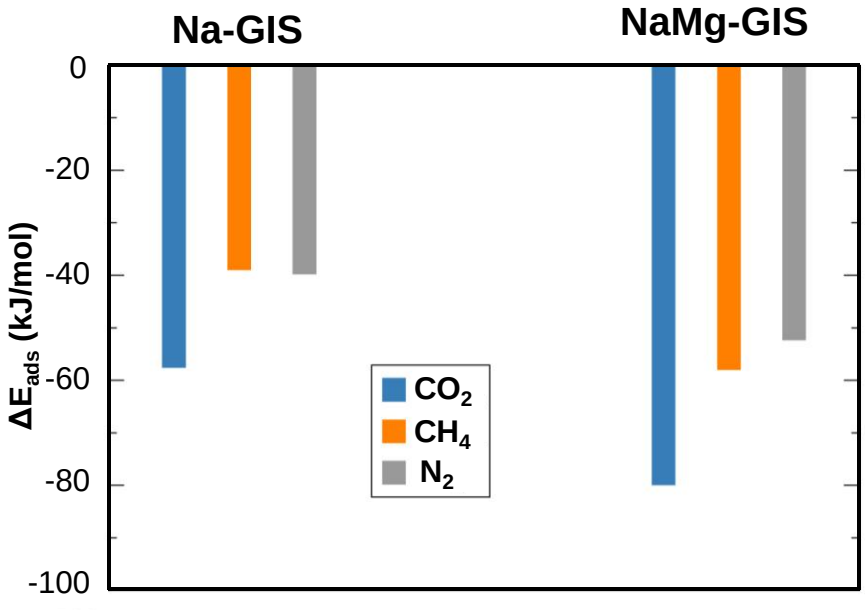

Figure 2. Adsorption energies of CO_2, CH_4, and N_2 in Na-GIS and NaMg-GIS at T = 0 K.

For all investigated molecules, adsorption was found to be stronger in NaMg-GIS as compared to Na-GIS, especially for CO_2. Indeed, the difference in adsorption energies between the pair CO_2-CH_4 and CO_2-N_2 increases from 18.6 to 22.0 kJ/mol (Na-GIS *vs* NaMg-GIS) and from 17.7 to 27.6 kJ/mol (Na-GIS *vs* NaMg-GIS), respectively. According to these results, a larger selectivity can thus be expected for CO_2/CH_4 and CO_2/N_2 separations performed using NaMg-GIS, compared to the pristine Na-GIS. For the adsorption of CO_2 in NaMg-GIS, different sites were tested to demonstrate the influence of the local cationic environment and to mimic different local exchange rates between Na^+ and Mg^{2+} that can be found in experiment samples (see Table S2). From these data, it is obvious that CO_2 adsorption is favored on Mg^{2+} sites, whereas the adsorption between two Na^+ cations and between one Na^+ and one Mg^{2+} is similar and less exothermic by about 20 kJ/mol. Adsorption on one Na^+ of NaMg-GIS is still less favorable. These results, further supported by in-house screening made on various elements (not shown), directed the choice of exchange with Mg^{2+} cations to evaluate the use of NaMg-GIS for enhanced CO_2/CH_4 and CO_2/N_2 separations.

3.2 Material Characterization

The XRD pattern of the as-synthesized Na-GIS, shown in Figure 3, is consistent with the NaP1 zeolite reported in the literature.[33] No additional peaks were observed in the X-ray diffractogram confirming the purity of the as-synthesized sample. Introducing Mg^{2+} cations into the GIS pore network changes the spatial distribution of the Na^+ extra-framework cations within the structure, as confirmed by the changes and the emergence of low-intensity peaks in the diffraction pattern. As expected, the diffraction pattern of NaMg3-GIS, exchanged three times with Mg^{2+}, showed more pronounced changes. Table S3 presents the unit cell composition of the three samples

calculated using ICP and EDS analysis. It reveals that the ion exchange of the parent Na-GIS with Mg^{2+} cations resulted in 30% degree of exchange for NaMg1-GIS and 50% for NaMg3-GIS. In a previous study made using Mg-exchange of MAP zeolite, achieving an exchange rate higher than 45% was found to be quite challenging.[52] Herein, with the procedure described above in the experimental section, it was possible to obtain an exchange of 50% in a reproducible fashion.

Scanning electron microscopy (SEM) analysis (Figure S6) revealed information about the crystal size and morphology of the GIS zeolite samples. Highly aggregated crystals with plate-like morphology were observed for the as-synthesized Na-GIS as well as for NaMg1-GIS and NaMg3-GIS, with crystal sizes ranging from 0.2 to 0.6 μm, confirming that the ion-exchange procedure did not alter the pristine particle shape and size of the samples.

N_2 adsorption-desorption isotherms measured at −196 °C revealed a rather low uptake of N_2 on both Na-GIS and NaMg1-GIS (Figure S7), indicating that the size of the pore apertures is too small to allow significant diffusion of N_2 into the pore network at cryogenic temperatures. This phenomenon was already observed and reported in the literature for GIS zeolites.[18,34] In the case of NaMg3-GIS, the pore windows of the GIS become highly inaccessible to N_2 molecules, resulting in extremely low surface area and pore volume. This effect is related to the large amount of Mg^{2+} cations present within the zeolite, resulting in a strong distortion of the 8MRs upon dehydration due to the smaller size and higher charge density of Mg^{2+}.

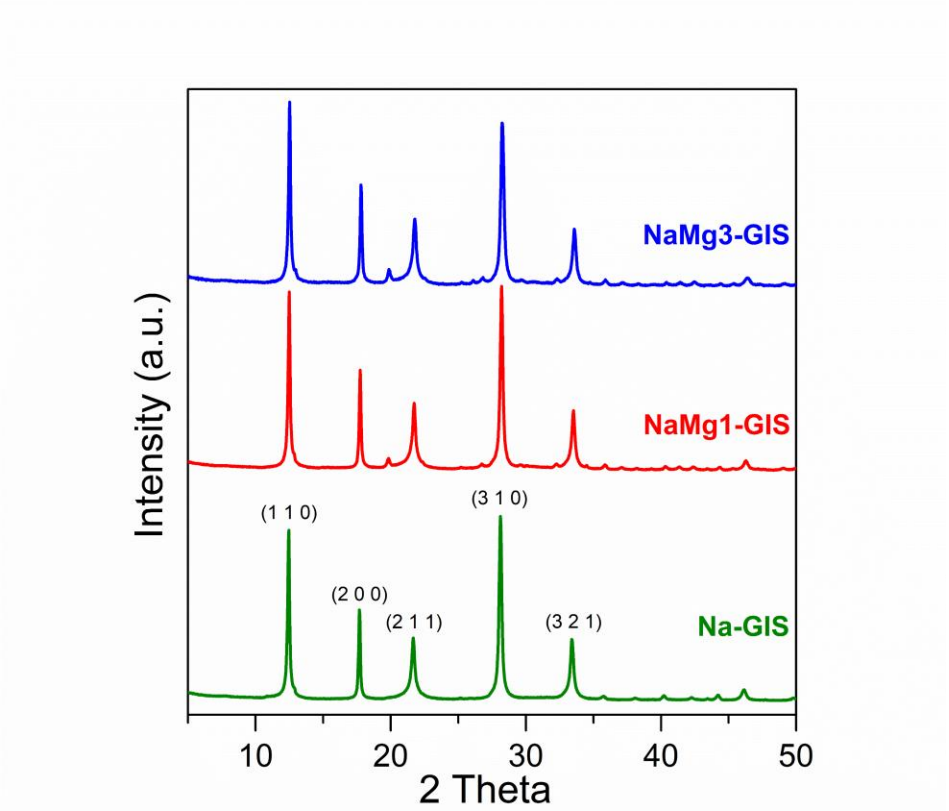

Figure 3. PXRD diffraction patterns of the as-synthesized Na-GIS, NaMg1-GIS, and NaMg3-GIS.

^{27}Al MAS NMR spectroscopic analysis of Na-GIS and NaMg1-GIS samples presented in Figure S8 reveals a single resonance at 58.5 ppm. This is consistent with the Al located in a tetrahedral coordination environment in the framework. The ^{29}Si MAS NMR spectra indicate the presence of four resonances at −93, −99, −103, and −110 ppm attributed to Si(nAl) coordination, where n corresponds to 3, 2, 1, and 0, respectively. Deconvolution and analysis of the ^{29}Si MAS NMR spectra resulted in framework Si/Al ratios of 3.00, 3.01, and 3.03 for Na-GIS, NaMg1-GIS, and NaMg3-GIS, respectively (Table S4). These findings are consistent with the Si/Al ratio determined from EDS and ICP-MS experiments (Table S3).

3.3 CO_2 adsorption

The CO_2 adsorption isotherms of Na-GIS and NaMg1-GIS at three different temperatures (0, 25, and 50 °C) are presented in Figure 4a and b. In contrast to the Type-I CO_2 adsorption isotherms of high aluminum zeolites (*e. g.* 13X), Na-GIS displays a hysteretic behavior and an adsorption step at low pressures, *i.e.*, approximately 0.02 bar at 0 °C. As the temperature increases to 50 °C, this step shifts from 0.02 to 0.2 bar. This is attributed to the change in the thermodynamic state of CO_2 as well as its adsorption mechanism on GIS-type zeolites. As described in earlier works, Na-GIS adsorbs CO_2 at low and high pressure following two different mechanisms denoted as the "gating cation" and "gate breathing" effects, respectively.[35] The latter phenomenon is related to the narrow-to-wide pore transition which has been described for several types of zeolites with flexible pore openings such as GIS,[35] MER,[53,54] and RHO.[55] The distribution of Na^+ cations at low pressure hinders the entry of guest molecules into the pore network of GIS. However, at high pressure, the redistribution of Na^+ cations causes the pore apertures to open, permitting the diffusion and adsorption of CO_2.

Unlike Na-GIS, the CO_2 adsorption isotherm of NaMg1-GIS exhibits a Type I isotherm across the temperature range of 0 to 50 °C. This is correlated with the reduced number of gating cations with high site occupancy within the 8MR windows in NaMg1-GIS, as 30% of the Na^+ cations have been replaced with Mg^{2+}, *i.e.*, 15% fewer extra-framework cations present in the channels. Moreover, Mg^{2+} cations can provide shorter distances of interaction with CO_2 and thus less steric effects than Na^+, depending on its coordination environment within the zeolite pores. An identical approach has been proposed to account for Type I isotherm behavior observed during CO_2 adsorption on Na-GIS with a Si/Al ratio of 4.7.[18] It should be noted that the partial exchange in the NaMg1-GIS structure has led to increased space in the GIS zeolite channels, which resulted in higher CO_2 uptake by 0.2 mmol/g at 25 °C and 1 bar as compared to the parent Na-GIS.

However, a further increase in the exchange of Na^+ with Mg^{2+} cations will reduce the proportion of gating cations with high site occupancy near the 8MRs even more. This might lead to lower CO_2 uptake because of the very pronounced pore network distortion. Indeed, the framework distortion increases with smaller and harder cations that coordinate more strongly to the zeolite framework oxygen.[18] This evolution is consistent with the adsorption behaviour observed for NaMg3-GIS with 50% of Na^+ cations exchanged where a low maximum of 1.55 mmol/g of CO_2 adsorbed at 25 °C and 1 bar was obtained (Figure S10). Moreover, when comparing the normalized time needed to reach the adsorption equilibrium as a function of the amount of Mg^{2+} present in the GIS zeolite, a clear trend appears where higher Mg^{2+} content always leads to longer adsorption times (Figure S11). Na-GIS exhibits the shortest adsorption time among the three studied samples, followed by NaMg1-GIS and NaMg3-GIS. It suggests that the presence of Mg^{2+} cations reduces the accessibility and/or the diffusion of CO_2 through the channels of an increasingly distorted GIS structure.

The calculated isosteric enthalpies of adsorption for CO_2 on the Na-GIS and NaMg1-GIS samples are shown in Figure S12. For Na-GIS, ΔH_{ads} was found to be relatively constant regardless of the investigated coverages, in the range of 42–44 kJ/mol, consistent with the previous values reported for Na-GIS (Si/Al = 2.5, 2.8), and which is characteristic of physisorption.[35] For NaMg1-GIS, the adsorption heat increased from around 42 to 56 kJ/mol as the adsorption amount increased from 0 to 1.5 mmol/g, remaining approximately at this value until 2.5 mmol/g. Such a pattern was already reported for nanosized Na-CHA[56] and Na-RHO[57]. The increase is generally related to the growing contribution of the adsorbate−adsorbent interactions until higher surface coverage is reached. Indeed, the adsorption of several CO_2 molecules onto Na^+ and/or Mg^{2+} is dominant until reaching a critical point where the loading is sufficient for the repulsive part of the CO_2−CO_2

contribution to be statistically relevant and to average the overall heat of adsorption values. However, it is important to underline that the cell distortion and accessibility/diffusion effects mentioned above resulting from the substantial presence of Mg^{2+} cations may also affect the ΔH_{ads} shape to some extent and that it is very difficult to isolate such contributions in the present case, due to the technical and kinetic limits associated with volumetric instrumentation up to 1 bar.

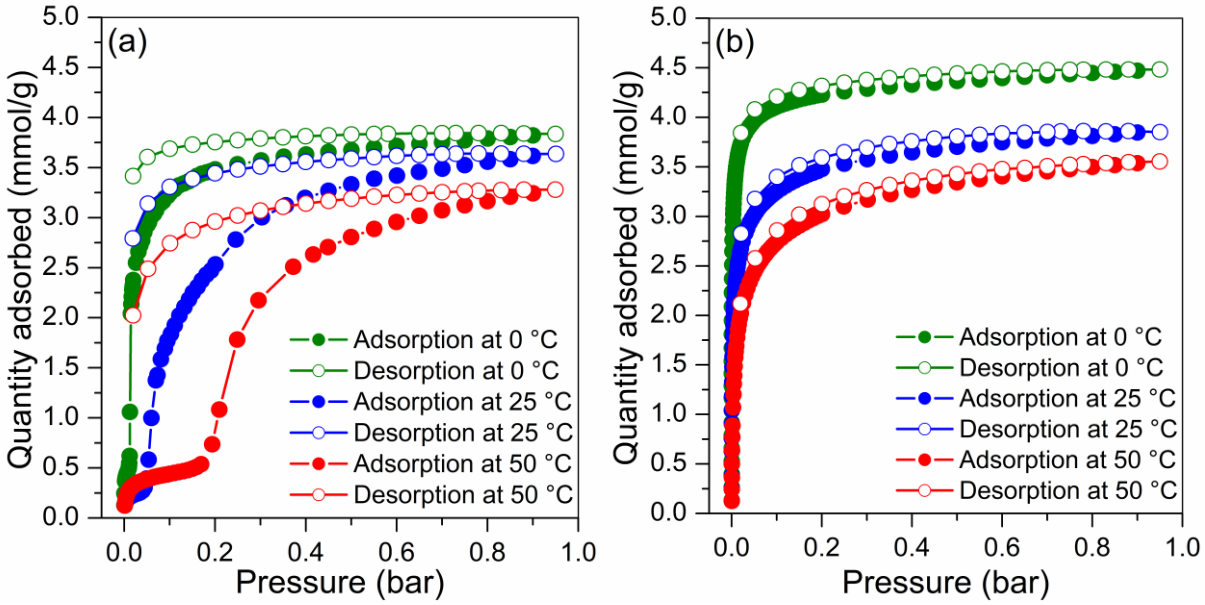

Figure 4. CO_2 adsorption-desorption isotherms at different temperatures on Na-GIS (a) and NaMg1-GIS (b).

Therefore, for a deeper understanding of the heat of adsorption behavior in NaMg1-GIS, the successive adsorption enthalpies, corresponding to isosteric adsorption enthalpies at different coverages,[51] have also been computed by *ab initio* molecular dynamics simulations at 300 K as described in the computational details. For consistency with the experimental data, CO_2 molecules were added successively up to 4 molecules per cell in Na-GIS and 2 in NaMg-GIS. In Na-GIS, the successive adsorption enthalpies are remarkably constant (in an interval of ± 4 kJ/mol around the average of 50 kJ/mol, see Figure 5a-c), as observed in the experimental data**,**

396 which can be related to a rather homogeneous environment of extra-framework Na^+ cations. In
397 NaMg-GIS, two independent simulations were performed to help the interpretation of the
398 experimental results. In one case, the first CO_2 molecule is adsorbed on a Na^+ cation and the
399 second one on a Mg^{2+}, while in the second case, the first CO_2 molecule is adsorbed on a Mg^{2+}
400 cation and the second one on a Na^+. The second case occurs spontaneously in simulations,
401 whereas the first requires checking if the CO_2 molecule remains on the Na^+ and restarting the run
402 if not. The two simulations gave the same total enthalpy of adsorption of two CO_2 molecules of
403 126 kJ/mol. If the first CO_2 molecule is adsorbed on a Na^+, the adsorption enthalpy is -51 ± 3
404 kJ/mol, and it increases (in absolute value) to -75 ± 3 kJ/mol for the second adsorption on a
405 Mg^{2+}. These data are consistent with the experimental results, confirming that the increase of the
406 isosteric heat of adsorption with the coverage could be related to accessibility issues of the guest
407 molecule to Mg^{2+} cations and the deformation of the framework in the presence of Mg^{2+}. Indeed,
408 in the P1 polymorph of the GIS, the pore openings are rather circular.[18] In contrast, optimized
409 structures of the P2 polymorphs of the Na-GIS and NaMg-GIS show ellipsoidal pores with much
410 distortion in the <010> direction compared to the <100> direction. Moreover, the network
411 distortion was much more pronounced for NaMg-GIS. In-depth investigations are ongoing on this
412 issue to reveal the importance of each contribution to the overall heat of adsorption curves.
413 However, these investigations go beyond the scope of the present manuscript and will be reported
414 in a dedicated adsorption and calorimetric study.

415

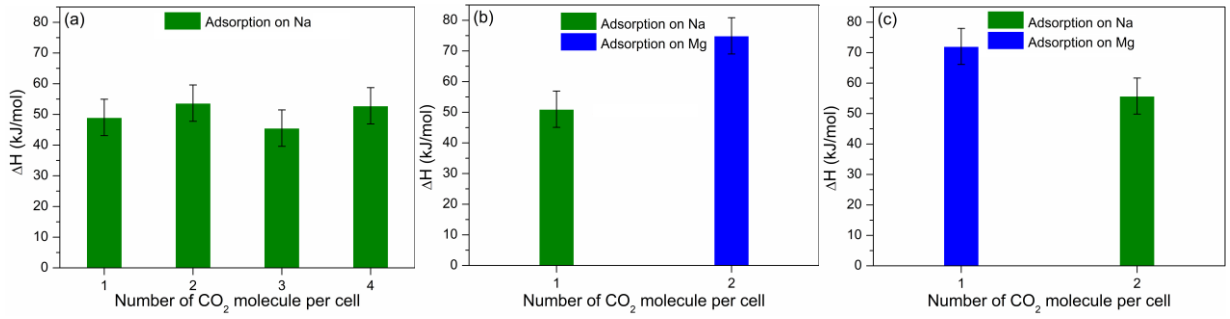

Figure 5. Successive enthalpies of adsorption (in kJ/mol) of CO_2 in (a) Na-GIS, (b) NaMg-GIS with a first adsorption on Na^+ and (c) NaMg-GIS with the first adsorption on Mg^{2+}, as a function of the number of CO_2 molecules per cell (1 CO_2/cell corresponding to 0.94 mmol/g in NaMg-GIS and 0.96 mmol/g in NaMg-GIS).

3.4 CO_2/N_2 and CO_2/CH_4 selectivities

In general, the quadrupole moment and the molecular sieving effect govern the selective adsorption of CO_2 in small pore zeolites (Table S5).[17,58] Moreover, for flexible zeolites, the "wide-to-narrow" effect results in pore shrinking, which hinders the adsorption of N_2 and CH_4 molecules.[59] Table 1 lists the CO_2/N_2 and CO_2/CH_4 ideal selectivities of Na-GIS, NaMg1-GIS and NaMg3-GIS based on their single component CO_2, N_2, and CH_4 equilibration adsorption isotherms measured at 25 °C and up to 1 bar (Figure 4, Figure S10 and S13). All materials exhibit significantly higher ideal selectivities towards CO_2 over N_2 (75, 117, and 81, respectively) and CH_4 (69,128 and 88, respectively). According to Choi *et al.*, the distortion of the GIS framework decreases as the cation size and softness increase.[18] From this effect, it would thus be expected that the framework of NaMg1-GIS distorts more during dehydration as compared to its parent Na-GIS, making it more difficult for N_2 and CH_4 to pass through the 8MR, ultimately resulting in lower adsorbed amounts for these gases. However, the even more pronounced distortion of the NaMg3-GIS structure also negatively affects the adsorption of CO_2, lowering the uptake and resulting in lower selectivities as compared to NaMg1-GIS. Thus, it appears that a "best-case

scenario" is offered by NaMg1-GIS that synergistically combines the advantages of the Mg cations and the underlying cell distortion.

Table 1. Adsorption capacities of CO_2, N_2 and CH_4 at 25 °C and 1 bar, and selectivity of CO_2/N_2 (15/85, v/v) and CO_2/CH_4 (40/60, v/v) on Na-GIS, NaMg1-GIS and NaMg3-GIS.

Sample	Adsorption capacity (mmol/g)			Selectivity	
	CO_2	N_2	CH_4	CO_2/N_2	CO_2/CH_4
Na-GIS	3.637	0.181	0.116	75	69
NaMg1-GIS	3.851	0.179	0.061	117	128
NaMg3-GIS	1.549	0.085	0.036	81	88

Figure 6a and b regroups the CO_2/CH_4 and CO_2/N_2 ideal separation performances (from the literature) of some of the best-performing porous materials, including activated carbon (AC)[60], metal-organic frameworks,[60–64] and zeolites.[65–72] The data was derived from static equilibrium sorption experiments. It reveals that Na-GIS and NaMg1-GIS exhibit relatively high CO_2 adsorption and one of the best CO_2/CH_4 and CO_2/N_2 selectivities. While one should keep in mind that comparison based solely on equilibrium data does not account for important effects seen in "real-world applications" such as accessibility and diffusion dynamics, it remains an essential facile preliminary step to predict the material's potential behavior and properties. Subsequently, in the upcoming section, we will focus on analyzing dynamic breakthrough curves performed under varying relevant conditions to clearly establish the true potential of NaMg-GIS materials.

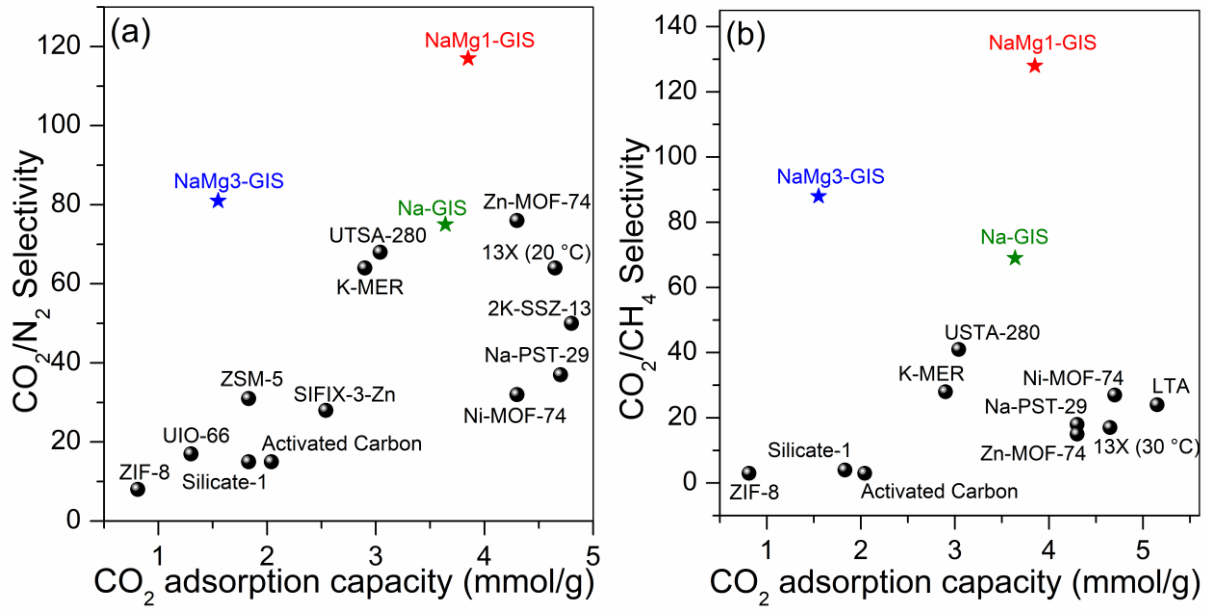

Figure 6. CO_2/N_2 (a) and CO_2/CH_4 (b) selectivity plotted against the adsorption capacity of CO_2 for a selection of porous materials. Most of the data was obtained using an online digitization tool.

3.5 Breakthrough curve analysis

To evaluate the samples in more realistic conditions and following the equilibrium adsorption characterization, the dynamic adsorption behavior of the different GIS samples was evaluated by breakthrough curve analysis using a ternary mixture of $He/N_2/CO_2$ (70/25/5 vol %) and $He/CH_4/CO_2$ (50/30/20 vol %) at 1 bar and 25 and 50 °C mimicking dry flue gas and biogas, respectively (Figure 7a-d). The difference in mass between the adsorbent, column, and water bath results in negligible changes to the temperature profile of the column throughout the whole breakthrough experiment (Figure S14 and S15). At 25 °C a slight temperature excursion of 0.15 and 0.20 °C was noted during the analysis of the CO_2/N_2 breakthrough curves and 0.25 and 0.35 °C during the analysis of the CO_2/CH_4 breakthrough curves for the Na-GIS and NaMg1-GIS respectively. At 50 °C no temperature deviation was observed. In the adsorption step of the breakthrough curve experiments using the $He/N_2/CO_2$ mixture (Figure S16), CO_2 breakthrough occurs at 27.5 and 21.6 min/g on NaMg1-GIS at 25 and 50 °C, respectively, which is longer than

for the parent Na-GIS (20.4 and 17.3 min/g, respectively). The CO_2 loadings calculated from breakthrough curve analysis (Table 2) for the NaMg1-GIS sample are consistent with the equilibrium adsorption isotherms, with an uptake of 3.01 mmol/g recorded at 0.05 bar, 25 °C and 2.44 mmol/g at 0.05 bar, 50 °C. While for Na-GIS, the CO_2 uptakes during the dynamic adsorption process were higher than expected based on the equilibrium isotherms (0.42 mmol/g recorded at 0.05 bar, 25 °C and 0.39 mmol/g at 0.05 bar, 50 °C). This could be attributed to residual water, which might have kept the pores slightly open for CO_2 adsorption, likely remaining due to the absence of a vacuum treatment during activation.

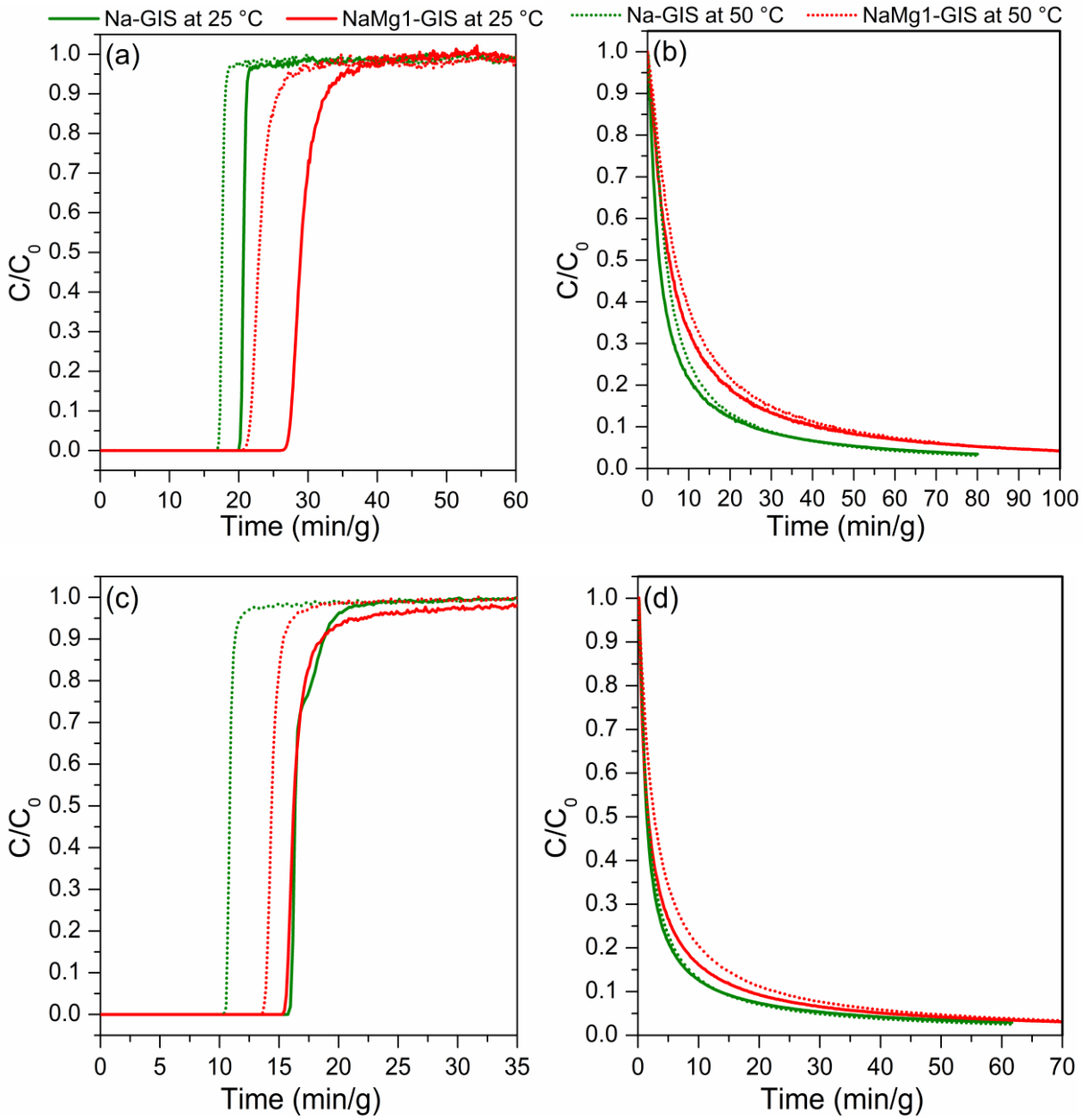

Figure 7. CO_2 breakthrough (a, c) and desorption curves (b, d) at 25 and 50 °C obtained from competitive dynamic adsorption experiments, CO_2/N_2/He, 5/25/70 (a,b) and CO_2/CH_4/He, 20/30/50 (c,d).

During the adsorption step using the He/CH_4/CO_2 mixture (Figure S16), similar breakthrough times for CO_2 of approximately 16 min/g were noted for both samples at 25 °C. However, at 50 °C, Na-GIS exhibits a shorter breakthrough time (10.6 min/g) as compared to NaMg1-GIS (13.7 min/g). The observed trend is consistent with the CO_2 loadings calculated from the breakthrough

curve analysis (Table 3). The calculated CO_2 loadings for the NaMg1-GIS compare well with the values from the equilibrium adsorption isotherms obtained at 0.2 bar of CO_2, 3.48 mmol/g at 25 °C and 3.02 mmol/g at 50 °C. Similar to the experiments in the presence of N_2, the Na-GIS sample exhibits significantly higher CO_2 loading under dynamic conditions compared to the values obtained from the equilibrium adsorption isotherms.

For the weakly adsorbing components, N_2 and CH_4, we observed near-instantaneous breakthrough of N_2 for both samples, while CH_4 took slightly longer. For both N_2 and CH_4 shorter breakthrough times were observed for NaMg1-GIS compared to Na-GIS. Both weak components displayed a roll-up feature in their respective breakthrough curves, indicative of their displacement from the adsorbent by CO_2 during the dynamic adsorption process. Because of this, we determined the adsorbed amounts of the weak components from the desorption curves. The calculations indicate extremely high selectivity towards CO_2 over the weak components (see Table 2 and 3).

One may also notice the distinct step in the breakthrough curve performed at 25 °C for the Na-GIS sample exposed to the He/CO_2/CH_4 mixture (Figure 7c). This phenomenon is attributed to the redistribution of Na^+ gating cations, which results in a pore opening that can accommodate CO_2, as discussed above.[18] The absence of this step at 50 °C is likely due to the low CO_2 partial pressure of 0.2 bar. In contrast, the step becomes apparent at pressures exceeding 0.2 bar at 50 °C, as indicated by the corresponding static adsorption isotherm (Figure 4a). Additional experiments (Figure S18 and S19) demonstrated that this step is only observable during the first cycle and only under high CO_2 partial pressure (P_{CO2} > 0.1 bar) conditions at 25 °C.

The desorption step was conducted under 100% He at the same flow rate used in the adsorption step. It was observed that the NaMg1-GIS sample took a longer time to achieve the desorption of

CO_2 ($C/C_0 < 0.05$) at 25 °C for the CO_2/N_2 mixture, with about 83 min/g compared to the parent Na-GIS (52 min/g). The same trend was observed in CO_2/CH_4 experiments, with 44 min/g of desorption time for NaMg1-GIS and 30 min/g for Na-GIS. However, desorption time remained unaffected upon elevating the temperature to 50 °C for both samples, with only a slight reduction of approximately 2 to 3 min/g observed across both samples and experimental setups.

Table 2. Adsorption capacity of CO_2 and N_2, and CO_2/N_2 molar selectivity for Na-GIS and NaMg1-GIS calculated from breakthrough curve analysis (CO_2/N_2/He: 5/25/70) at 25 and 50 °C at saturation.

Temperature (°C)	Na-GIS			NaMg1-GIS		
	Capacity (mmol/g)		Selectivity	Capacity (mmol/g)		Selectivity
	CO_2	N_2		CO_2	N_2	
25	1.727	0.048	180	3.012	0.009	1673
50	1.292	0.021	308	2.246	0.009	1248

The adsorption capacity of CO_2 at saturation typically decreases as the temperature increases from 25 to 50 °C, as indicated in Tables 2 and 3. Both GIS samples showed comparable trends in selectivity towards CO_2/N_2 and CO_2/CH_4, with a decrease observed as the temperature rises from 25 to 50 °C. Overall, the NaMg1-GIS sample exhibits a superior capacity for CO_2 adsorption, a lower N_2 adsorption capacity, and negligible adsorption of CH_4. Consequently, under dynamic adsorption conditions, NaMg1-GIS always exhibits a higher selectivity for CO_2 over N_2 and considerably greater selectivity for CO_2 over CH_4 than the parent Na-GIS sample. This finding holds considerable significance for CO_2 separation applications, as NaMg1-GIS was more effective in selectively capturing CO_2 from mixed gas streams.

Table 3. Adsorption capacity of CO_2 and CH_4, and CO_2/CH_4 molar selectivity for Na-GIS and NaMg1-GIS calculated from breakthrough curve analysis (CO_2/CH_4/He: 20/30/50) at 25 and 50 °C at saturation.

Temperature (°C)	Na-GIS			NaMg1-GIS		
	Capacity (mmol/g)		Selectivity	Capacity (mmol/g)		Selectivity
	CO_2	CH_4		CO_2	CH_4	

25	2.930	0.051	86	3.062	≈ 0	-
50	1.64	0.042	59	2.801	≈ 0	-

To further validate the suitability of the GIS samples for separation processes, simplified fast cycling experiments consisting of five cycles of 100 seconds of adsorption followed by 300 seconds of desorption in $CO_2/N_2/He$ or $CO_2/CH_4/He$ mixtures for both Na-GIS and NaMg1-GIS samples were conducted (Figure S20 and S21). It is to be noted that in order to consider an unfavourable scenario, no PSA or TSA was used for desorption. The desorption was only performed by reverting the gas flow to 100% He, which does not favour fast and efficient desorption. The experimental results reveal that after 5 cycles, virtually no CO_2 (below 0.1 %) is seen during the desorption at both temperatures (25 and 50 °C) for NaMg1-GIS, whereas about 2–3 % CO_2 was observed at the beginning of the desorption step after 2 and 1 cycles at 25 and 50 °C, respectively, for the parent Na-GIS material confirming the higher separation performance of the Mg-exchanged GIS in cycling conditions. Similar observations were made in the case of CO_2/CH_4 separation, to a lesser extent. Indeed, NaMg1-GIS demonstrated the ability to generate pure CH_4 before CO_2 starts to elute from the columnduring the desorption of the third cycle, as compared to Na-GIS where CO_2 elutes during the desorption of the second and first cycle at 25 and 50 °C respectively. These findings show that NaMg1-GIS zeolite exhibits promising potential for efficient CO_2 separation in fast cycling conditions, outperforming the parent Na-GIS in both CO_2/CH_4 and CO_2/N_2 binary systems.

4. Conclusions

Partially exchanged NaMg1-GIS and NaMg3-GIS, with 30% and 50% degree of exchange, respectively, have been investigated as potentially promising selective CO_2 adsorbents for carbon capture from flue gas and biogas. In contrast to as-synthesized Na-GIS, whose isotherm exhibits

a low-pressure step at 0.02 bar at 25 °C, the Mg^{2+}-containing counterpart exhibits a classical Type I isotherm. Our findings demonstrate that NaMg1-GIS, with a lower Mg^{2+} content (30%), exhibits remarkable CO_2 adsorption capacity and selectivity towards CO_2/N_2 and CO_2/CH_4. On the other hand, NaMg3-GIS, with a higher Mg^{2+} content (50%), displays reduced CO_2 adsorption and lower CO_2/N_2 and CO_2/CH_4 selectivities due to restricted access to the pore network. DFT calculations supported these conclusions, confirming that adsorption is stronger on Mg^{2+} than on Na^+ extra-framework cations and that accessibility issues appear on NaMg-GIS with higher Mg^{2+} concentration. The presence of charge-balancing Mg^{2+} leads to a distortion in the framework pore structure, which hinders the adsorption of N_2 and CH_4. The degree of this distortion is directly influenced by the Mg^{2+} concentration, with higher Mg^{2+} contents resulting in greater pore structure distortion and, subsequently, lower CO_2 adsorption. In agreement with single component adsorption results, dynamic CO_2/N_2 and CO_2/CH_4 breakthrough curve analysis revealed that NaMg1-GIS displays high CO_2 adsorption capacity with higher selectivity toward CO_2 over N_2 and CH_4 compared with the all-sodium GIS. The framework pore distortion induced by the presence of Mg^{2+} impairs the diffusion of CO_2 through the 8-membered ring window leading to better dynamic adsorption/separation properties. Further investigations are needed to understand the effect of the bivalent cation on the zeolite structure and to enhance the adsorption capacity and selectivity of these materials, particularly for CO_2 capture purposes.

AUTHOR INFORMATION

Corresponding Authors

*E-mail : valentin.valtchev@ensicaen.f

*E-mail : remy.guillet-nicolas@ensicaen.fr

Notes

The authors declare no competing financial interest.

ASSOCIATED CONTENT

Supporting information. Contains information pertaining to breakthrough curve area determination, variable temperature XRD patterns, CO_2 adsorption configuration models, SEM images, ^{27}Al and ^{29}Si NMR spectra, TG analysis, CO_2, N_2, and CH_4 adsorption isotherms, the entire competitive dynamic adsorption step, and adorption energies and enthalpies details.

Acknowledgments

This study was partially sponsored by the Industrial Chair (TotalEnergies – Region of Normandy; n°CCR_ECOGAS2022; TOTE: CT00000759-1). VV acknowledges support from the European Union-NextGenerationEU, through the National Recovery and Resilience Plan of the Republic of Bulgaria, project No BG-RRP-2.004-0008.

References

(1) Yoro, K. O.; Daramola, M. O. CO_2 Emission Sources, Greenhouse Gases, and the Global Warming Effect. In *Advances in Carbon Capture*; Elsevier, 2020; pp 3–28.

(2) Lin, Q.; Zhang, X.; Wang, T.; Zheng, C.; Gao, X. Technical Perspective of Carbon Capture, Utilization, and Storage. *Engineering* **2022**, *14*, 27–32.

(3) Zhang, J.; Yedlapalli, P.; Lee, J. W. Thermodynamic Analysis of Hydrate-Based Pre-Combustion Capture of CO_2. *Chem. Eng. Sci.* **2009**, *64* (22), 4732–4736.

(4) Yamada, H. Amine-Based Capture of CO_2 for Utilization and Storage. *Polym. J.* **2021**, *53* (1), 93–102.

(5) Yang, H.; Xu, Z.; Fan, M.; Gupta, R.; Slimane, R. B.; Bland, A. E.; Wright, I. Progress in Carbon Dioxide Separation and Capture: A Review. *J. Environ. Sci.* **2008**, *20* (1), 14–27.

(6) Ding, M.; Liu, X.; Ma, P.; Yao, J. Porous Materials for Capture and Catalytic Conversion of CO_2 at Low Concentration. *Coord. Chem. Rev.* **2022**, *465*, 214576.

(7) Gutierrez-Ortega, A.; Montes-Morán, M. A.; Parra, J. B.; Sempere, J.; Nomen, R.; Gonzalez-Olmos, R. Comparative Study of Binderless Zeolites and Carbon Molecular Sieves as Adsorbents for CO_2 Capture Processes. *J. CO_2 Util.* **2022**, *61*, 102012.

(8) Kemp, K. C.; Min, J. G.; Choi, H. J.; Hong, S. B. Small Gas Adsorption and Separation in Small-Pore Zeolites. In *New Developments in Adsorption/Separation of Small Molecules by Zeolites*; Valencia, S., Rey, F., Eds.; Structure and Bonding; Springer International Publishing: Cham, 2020; Vol. 184, pp 1–30.

(9) Remy, T.; Peter, S. A.; Van Tendeloo, L.; Van der Perre, S.; Lorgouilloux, Y.; Kirschhock, C. E. A.; Baron, G. V.; Denayer, J. F. M. Adsorption and Separation of CO_2 on KFI Zeolites: Effect of Cation Type and Si/Al Ratio on Equilibrium and Kinetic Properties. *Langmuir* **2013**, *29* (16), 4998–5012.

(10) Wang, L.; Liu, J.; Lin, C.; Shang, H.; Yang, J.; Li, L.; Li, J. Effects of Different Alkali Metal Cations in FAU Zeolites on the Separation Performance of CO_2/N_2O. *Chem. Eng. J.* **2022**, *431*, 134257.

(11) Yang, J.; Shang, H.; Krishna, R.; Wang, Y.; Ouyang, K.; Li, J. Adjusting the Proportions of Extra-Framework K^+ and Cs^+ Cations to Construct a "Molecular Gate" on ZK-5 for CO_2 Removal. *Microporous Mesoporous Mater.* **2018**, *268*, 50–57.

(12) Yang, J.; Zhao, Q.; Xu, H.; Li, L.; Dong, J.; Li, J. Adsorption of CO_2 , CH_4 , and N_2 on Gas Diameter Grade Ion-Exchange Small Pore Zeolites. *J. Chem. Eng. Data* **2012**, *57* (12), 3701–3709.

(13) Debost, M.; Clatworthy, E. B.; Grand, J.; Barrier, N.; Nesterenko, N.; Gilson, J.-P.; Boullay, P.; Mintova, S. Direct Synthesis of Nanosized CHA Zeolite Free of Organic Template by a Combination of Cations as Structure Directing Agents. *Microporous Mesoporous Mater.* **2023**, *358*, 112337.

(14) Fischer, M.; Bell, R. G. Influence of Zeolite Topology on CO_2/N_2 Separation Behavior: Force-Field Simulations Using a DFT-Derived Charge Model. *J. Phys. Chem. C* **2012**, *116* (50), 26449–26463.

(15) Bonenfant, D.; Kharoune, M.; Niquette, P.; Mimeault, M.; Hausler, R. Advances in Principal Factors Influencing Carbon Dioxide Adsorption on Zeolites. *Sci. Technol. Adv. Mater.* **2008**, *9* (1), 013007.

(16) Gouveia, L. G. T.; Agustini, C. B.; Perez-Lopez, O. W.; Gutterres, M. CO_2 Adsorption Using Solids with Different Surface and Acid-Base Properties. *J. Environ. Chem. Eng.* **2020**, *8* (4), 103823.

(17) Walton, K. S.; Abney, M. B.; Douglas LeVan, M. CO_2 Adsorption in Y and X Zeolites Modified by Alkali Metal Cation Exchange. *Microporous Mesoporous Mater.* **2006**, *91* (1–3), 78–84.

(18) Choi, H. J.; Min, J. G.; Ahn, S. H.; Shin, J.; Hong, S. B.; Radhakrishnan, S.; Chandran, C. V.; Bell, R. G.; Breynaert, E.; Kirschhock, C. E. A. Framework Flexibility-Driven CO_2 Adsorption on a Zeolite. *Mater. Horiz.* **2020**, *7* (6), 1528–1532.

(19) Deka, R. C.; Kinkar Roy, R.; Hirao, K. Basicity of the Framework Oxygen Atom of Alkali and Alkaline Earth-Exchanged Zeolites: A Hard–Soft Acid–Base Approach. *Chem. Phys. Lett.* **2000**, *332* (5–6), 576–582.

(20) Shang, J.; Li, G.; Singh, R.; Gu, Q.; Nairn, K. M.; Bastow, T. J.; Medhekar, N.; Doherty, C. M.; Hill, A. J.; Liu, J. Z.; Webley, P. A. Discriminative Separation of Gases by a "Molecular Trapdoor" Mechanism in Chabazite Zeolites. *J. Am. Chem. Soc.* **2012**, *134* (46), 19246–19253.

(21) Shang, J.; Li, G.; Singh, R.; Xiao, P.; Liu, J. Z.; Webley, P. A. Determination of Composition Range for "Molecular Trapdoor" Effect in Chabazite Zeolite. *J. Phys. Chem. C* **2013**, *117* (24), 12841–12847.

(22) Liu, Q.; Pham, T.; Porosoff, M. D.; Lobo, R. F. ZK-5: A CO_2 -Selective Zeolite with High Working Capacity at Ambient Temperature and Pressure. *ChemSusChem* **2012**, *5* (11), 2237–2242.

(23) Bower, J. K.; Barpaga, D.; Prodinger, S.; Krishna, R.; Schaef, H. T.; McGrail, B. P.; Derewinski, M. A.; Motkuri, R. K. Dynamic Adsorption of CO_2/N_2 on Cation-Exchanged Chabazite SSZ-13: A Breakthrough Analysis. *ACS Appl. Mater. Interfaces* **2018**, *10* (17), 14287–14291.

(24) Aly, E.; Zafanelli, L. F. A. S.; Henrique, A.; Golini Pires, M.; Rodrigues, A. E.; Gleichmann, K.; Silva, J. A. C. Fixed Bed Adsorption of CO_2, CH_4, and N_2 and Their Mixtures in Potassium-Exchanged Binder-Free Beads of Y Zeolite. *Ind. Eng. Chem. Res.* **2021**, *60* (42), 15236–15247.

(25) Sheikholeslami, F.; Fatemi, S. Efficient Separation of CO_2 from Methane at High Pressures by Modified Microporous Titanosilicates; Design and Breakthrough Studies. *Fuel* **2023**, *334*, 126673.

(26) Wu, L.; Liu, J.; Shang, H.; Li, S.; Yang, J.; Li, L.; Li, J. Capture CO_2 from N_2 and CH_4 by Zeolite L with Different Crystal Morphology. *Microporous Mesoporous Mater.* **2021**, *316*, 110956.

(27) Adams, C. J.; Araya, A.; Cunningham, K. J.; Franklin, K. R.; White, I. F. Measurement and Prediction of Ca–Na Ion-Exchangeequilibrium in Maximum Aluminium P (MAP), a Zeolite with the GISframework Topology. *J. Chem. Soc. Faraday Trans.* **1997**, *93* (3), 499–503.

(28) Grice, J. D.; Rowe, R.; Poirier, G. Garronite-Na, a New Zeolite Species from Mont Saint-Hilaire, QuÉbec. *Can. Mineral.* **2016**, *54* (6), 1549–1562.

(29) Alberti, A.; Vezzalini, G. The Crystal Structure of Amicite, a Zeolite. *Acta Crystallogr. B* **1979**, *35* (12), 2866–2869.

(30) Fischer, K. The Crystal Structure Determination of the Zeolite Gismondite. $CaAl_2Si_2O_8 \cdot 4H_2O$. *Am. Mineral.* **1963**, *48* (5–6), 664–672.

(31) Skrzyńska, K.; Cametti, G.; Galuskina, I. O.; Vapnik, Y.; Galuskin, E. V. Gismondine-Sr, $Sr_4(Al_8Si_8O_{32}) \cdot 9H_2O$, a New Strontium Dominant, Orthorhombic Zeolite of the Gismondine Series from the Hatrurim Complex, Israel. *Am. Mineral.* **2023**, *108* (2), 249–258.

(32) Baur, W. H.; Fischer, R. X. *The Flexibility of the T-X-T Hinges between the Coordination Tetrahedra in Various Zeolitic Frameworks. An Empirical Structural Study.*; preprint; In Review, 2022.

(33) Guo, J.-C.; Zou, C.; Chiang, C.-Y.; Chang, T.-A.; Chen, J.-J.; Lin, L.-C.; Kang, D.-Y. NaP1 Zeolite Membranes with High Selectivity for Water-Alcohol Pervaporation. *J. Membr. Sci.* **2021**, *639*, 119762.

(34) Oleksiak, M. D.; Ghorbanpour, A.; Conato, M. T.; McGrail, B. P.; Grabow, L. C.; Motkuri, R. K.; Rimer, J. D. Synthesis Strategies for Ultrastable Zeolite GIS Polymorphs as Sorbents for Selective Separations. *Chem. – Eur. J.* **2016**, *22* (45), 16078–16088.

(35) Choi, H. J.; Hong, S. B. Effect of Framework Si/Al Ratio on the Mechanism of CO_2 Adsorption on the Small-Pore Zeolite Gismondine. *Chem. Eng. J.* **2022**, *433*, 133800.

(36) Cheung, O.; Hedin, N. Zeolites and Related Sorbents with Narrow Pores for CO_2 Separation from Flue Gas. *RSC Adv.* **2014**, *4* (28), 14480–14494.

(37) Bao, Z.; Yu, L.; Ren, Q.; Lu, X.; Deng, S. Adsorption of CO_2 and CH_4 on a Magnesium-Based Metal Organic Framework. *J. Colloid Interface Sci.* **2011**, *353* (2), 549–556.

(38) Clatworthy, E. B.; Ghojavand, S.; Guillet-Nicolas, R.; Gilson, J.-P.; Llewellyn, P. L.; Nesterenko, N.; Mintova, S. Dynamic Adsorption of CO_2 by CHA Zeolites – Size Matters. *Chem. Eng. J.* **2023**, *471*, 144557.

(39) Kresse, G.; Hafner, J. Ab Initio Molecular Dynamics for Liquid Metals. *Phys. Rev. B* **1993**, *47* (1), 558–561.

(40) Kresse, G.; Hafner, J. Ab Initio Molecular-Dynamics Simulation of the Liquid-Metal–Amorphous-Semiconductor Transition in Germanium. *Phys. Rev. B* **1994**, *49* (20), 14251–14269.

(41) Kresse, G.; Furthmüller, J. Efficient Iterative Schemes for Ab Initio Total-Energy Calculations Using a Plane-Wave Basis Set. *Phys. Rev. B* **1996**, *54* (16), 11169–11186.

(42) Blöchl, P. E. Projector Augmented-Wave Method. *Phys Rev B* **1994**, *50* (24), 17953–17979.

(43) Kresse, G.; Joubert, D. From Ultrasoft Pseudopotentials to the Projector Augmented-Wave Method. *Phys. Rev. B* **1999**, *59* (3), 1758–1775.

(44) Perdew, J. P.; Burke, K.; Ernzerhof, M. Generalized Gradient Approximation Made Simple. *Phys. Rev. Lett.* **1996**, *77* (18), 3865–3868.

(45) Grimme, S.; Antony, J.; Ehrlich, S.; Krieg, H. A Consistent and Accurate Ab Initio Parametrization of Density Functional Dispersion Correction (DFT-D) for the 94 Elements H-Pu. *J. Chem. Phys.* **2010**, *132* (15), 154104.

(46) Grimme, S.; Ehrlich, S.; Goerigk, L. Effect of the Damping Function in Dispersion Corrected Density Functional Theory. *J. Comput. Chem.* **2011**, *32* (7), 1456–1465.

(47) Delachaux, F.; Hessou, E. P.; Vallières, C.; Monnier, H.; Badawi, M. A Dispersion-Corrected DFT Method for Zeolite-Based CO_2/N_2 Separation: Assessment and Application. *J. Environ. Chem. Eng.* **2023**, *11* (1), 109052.

(48) Berro, Y.; Badawi, M.; El Haj Hassan, F.; Kassir, M.; Tielens, F. Water-Silanol Interactions on the Amorphous Silica Surface: A Dispersion-Corrected DFT Investigation. *J. Mol. Liq.* **2020**, *320*, 114496.

(49) Andersen, H. C. Molecular Dynamics Simulations at Constant Pressure and/or Temperature. *J. Chem. Phys.* **1980**, *72* (4), 2384–2393.

(50) Frenkel, D.; Smit, B. *Understanding Molecular Simulation*; Computational science series; Academic Press, 2002.

(51) Foucaud, Y.; Ben Jannet, A.; Caramori, S.; Canevesi, R.; Said, M.; Celzard, A.; Fierro, V.; Badawi, M.; Pastore, M. Hydration Mechanisms of Tungsten Trioxide Revealed by Water Adsorption Isotherms and First-Principles Molecular Dynamics Simulations. *J. Phys. Chem. C* **2023**, *127* (11), 5584–5596.

(52) Allen, S.; Carr, S.; Chapple, A.; Dyer, A.; Heywood, B. Ion Exchange in the Synthetic Gismondine, Zeolite MAP. *Phys. Chem. Chem. Phys.* **2002**, *4* (11), 2409–2415.

(53) Georgieva, V. M.; Bruce, E. L.; Verbraeken, M. C.; Scott, A. R.; Casteel, W. J. Jr.; Brandani, S.; Wright, P. A. Triggered Gate Opening and Breathing Effects during Selective CO_2 Adsorption by Merlinoite Zeolite. *J. Am. Chem. Soc.* **2019**, *141* (32), 12744–12759.

(54) Georgieva, V. M.; Bruce, E. L.; Chitac, R. G.; Lozinska, M. M.; Hall, A. M.; Murray, C. A.; Smith, R. I.; Turrina, A.; Wright, P. A. Cation Control of Cooperative CO_2 Adsorption in Li-Containing Mixed Cation Forms of the Flexible Zeolite Merlinoite. *Chem. Mater.* **2021**, *33* (4), 1157–1173.

(55) Verbraeken, M. C.; Mennitto, R.; Georgieva, V. M.; Bruce, E. L.; Greenaway, A. G.; Cox, P. A.; Min, J. G.; Hong, S. B.; Wright, P. A.; Brandani, S. Understanding CO_2 Adsorption in a Flexible Zeolite through a Combination of Structural, Kinetic and Modelling Techniques. *Sep. Purif. Technol.* **2021**, *256*, 117846.

(56) Ghojavand, S.; Coasne, B.; Clatworthy, E. B.; Guillet-Nicolas, R.; Bazin, P.; Desmurs, M.; Jacobo Aguilera, L.; Ruaux, V.; Mintova, S. Alkali Metal Cations Influence the CO_2 Adsorption Capacity of Nanosized Chabazite: Modeling vs Experiment. *ACS Appl. Nano Mater.* **2022**, *5* (4), 5578–5588.

(57) Lozinska, M. M.; Mowat, J. P. S.; Wright, P. A.; Thompson, S. P.; Jorda, J. L.; Palomino, M.; Valencia, S.; Rey, F. Cation Gating and Relocation during the Highly Selective "Trapdoor" Adsorption of CO_2 on Univalent Cation Forms of Zeolite Rho. *Chem. Mater.* **2014**, *26* (6), 2052–2061.

(58) Kim, H.; Cho, H. S.; Kim, C.; Choi, M. Gradual Disordering of LTA Zeolite for Continuous Tuning of the Molecular Sieving Effect. *J. Phys. Chem. C* **2017**, *121* (12), 6807–6812.

(59) Fu, D.; Davis, M. E. Carbon Dioxide Capture with Zeotype Materials. *Chem. Soc. Rev.* **2022**, *51* (22), 9340–9370.

(60) McEwen, J.; Hayman, J.-D.; Ozgur Yazaydin, A. A Comparative Study of CO_2, CH_4 and N_2 Adsorption in ZIF-8, Zeolite-13X and BPL Activated Carbon. *Chem. Phys.* **2013**, *412*, 72–76.

(61) Lin, R.-B.; Li, L.; Alsalme, A.; Chen, B. An Ultramicroporous Metal–Organic Framework for Sieving Separation of Carbon Dioxide from Methane. *Small Struct.* **2020**, *1* (3), 2000022.

(62) Nugent, P.; Belmabkhout, Y.; Burd, S. D.; Cairns, A. J.; Luebke, R.; Forrest, K.; Pham, T.; Ma, S.; Space, B.; Wojtas, L.; Eddaoudi, M.; Zaworotko, M. J. Porous Materials with Optimal Adsorption Thermodynamics and Kinetics for CO_2 Separation. *Nature* **2013**, *495* (7439), 80–84.

(63) Hu, Z.; Peng, Y.; Kang, Z.; Qian, Y.; Zhao, D. A Modulated Hydrothermal (MHT) Approach for the Facile Synthesis of UiO-66-Type MOFs. *Inorg. Chem.* **2015**, *54* (10), 4862–4868.

(64) Zhang, X.; Zheng, Q.; He, H. Multicomponent Adsorptive Separation of CO_2, CH_4, N_2, and H2 over M-MOF-74 and AX-21@M-MOF-74 Composite Adsorbents. *Microporous Mesoporous Mater.* **2022**, *336*, 111899.

(65) Choi, H. J.; Jo, D.; Min, J. G.; Hong, S. B. The Origin of Selective Adsorption of CO_2 on Merlinoite Zeolites. *Angew. Chem. Int. Ed.* **2021**, *60* (8), 4307–4314.

(66) Lee, H.; Shin, J.; Choi, W.; Choi, H. J.; Yang, T.; Zou, X.; Hong, S. B. PST-29: A Missing Member of the RHO Family of Embedded Isoreticular Zeolites. *Chem. Mater.* **2018**, *30* (19), 6619–6623.

(67) Yang, J.; Yuan, N.; Xu, M.; Liu, J.; Li, J.; Deng, S. Enhanced Mass Transfer on Hierarchical Porous Pure Silica Zeolite Used for Gas Separation. *Microporous Mesoporous Mater.* **2018**, *266*, 56–63.

(68) Park, Y.; Ju, Y.; Park, D.; Lee, C.-H. Adsorption Equilibria and Kinetics of Six Pure Gases on Pelletized Zeolite 13X up to 1.0 MPa: CO_2, CO, N_2, CH_4, Ar and H_2. *Chem. Eng. J.* **2016**, *292*, 348–365.

(69) Liu, Q.; He, P.; Qian, X.; Fei, Z.; Zhang, Z.; Chen, X.; Tang, J.; Cui, M.; Qiao, X.; Shi, Y. Enhanced CO_2 Adsorption Performance on Hierarchical Porous ZSM-5 Zeolite. *Energy Fuels* **2017**, *31* (12), 13933–13941.

(70) Gong, J.; Wang, C.; Zeng, C.; Zhang, L. Hydrothermal Preparation of Hierarchical SAPO-34 Constructed by Nano-Sheets Using Rapeseed Pollen Extract as Water and Its CO_2 Adsorption Property. *Microporous Mesoporous Mater.* **2016**, *221*, 128–136.

(71) Xu, X.; Zhao, X.; Sun, L.; Liu, X. Adsorption Separation of Carbon Dioxide, Methane and Nitrogen on Monoethanol Amine Modified β-Zeolite. *J. Nat. Gas Chem.* **2009**, *18* (2), 167–172.

(72) Palomino, M.; Corma, A.; Rey, F.; Valencia, S. New Insights on CO_2 −Methane Separation Using LTA Zeolites with Different Si/Al Ratios and a First Comparison with MOFs. *Langmuir* **2010**, *26* (3), 1910–1917.